



HAL
open science

Marine corrosion resistance of CeO₂/Mg(OH)₂ mixed coating on a low alloyed steel

K. Aggoun, L. Chaal, Jordi Creus, R. Sabot, B. Saidani, Marc Jeannin

► **To cite this version:**

K. Aggoun, L. Chaal, Jordi Creus, R. Sabot, B. Saidani, et al.. Marine corrosion resistance of CeO₂/Mg(OH)₂ mixed coating on a low alloyed steel. *Surface and Coatings Technology*, 2019, 372, pp.410-421. 10.1016/j.surfcoat.2019.05.053 . hal-02478150

HAL Id: hal-02478150

<https://hal.science/hal-02478150>

Submitted on 25 Oct 2021

HAL is a multi-disciplinary open access archive for the deposit and dissemination of scientific research documents, whether they are published or not. The documents may come from teaching and research institutions in France or abroad, or from public or private research centers.

L'archive ouverte pluridisciplinaire **HAL**, est destinée au dépôt et à la diffusion de documents scientifiques de niveau recherche, publiés ou non, émanant des établissements d'enseignement et de recherche français ou étrangers, des laboratoires publics ou privés.



Distributed under a Creative Commons Attribution - NonCommercial 4.0 International License

Marine corrosion resistance of CeO₂ / Mg(OH)₂ mixed coating on a low alloyed steel

Authors: K. Aggoun^{1,2}, L. Chaal², J. Creus¹, R. Sabot¹, B. Saidani², M. Jeannin^{1,*}

(1) Laboratoire des Sciences de l'Ingénieur pour l'Environnement (LaSIE) UMR CNRS 7356
– University of La Rochelle, Av. Michel Crépeau, 17042 LA ROCHELLE, France.

(2) Laboratoire d'Electrochimie, Corrosion et de Valorisation Energétique (LECVE), Faculté de Technologie, University of Bejaia (06000), Algeria.

(*) corresponding author: marc.jeannin@univ-lr.fr

Abstract

Mixed Mg(OH)₂ / CeO₂ coatings were deposited by cathodic electrodeposition on AISI 4135 steel in order to improve its resistance to marine corrosion. CeO₂ coating was first prepared by cathodic electrodeposition in a low concentration of cerium nitrate bath. Then, brucite layer is formed by cathodic polarization in magnesium nitrate bath. Scanning electronic microscope (SEM), energy dispersive X-ray spectroscopy (EDS), X-ray diffraction (XRD) and micro-Raman spectroscopy (μ -Raman) analysis were used to study the morphology, chemical composition, microstructure and thickness of the coatings. The corrosion resistance of the coatings was evaluated in artificial seawater by electrochemical methods. CeO₂ coating present a porous and cracked structure; consequently, it offers low corrosion protection of steel in seawater. However, Mg(OH)₂ / CeO₂ mixed coatings have a more uniform and compact structure and present a better corrosion protection of steel in seawater. The protection efficiency of these coatings is then discussed and a protection mechanism is proposed after surface and cross-section SEM and μ -Raman analyses of the coating after several seawater immersion durations.

Key words: steel, cerium oxide, magnesium hydroxide, coating, marine corrosion.

1. Introduction

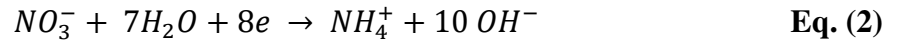
Currently, surface treatments are considered as an essential industrial process to improve the functional properties of metals, including corrosion resistance. Among the various treatment process, chromium based conversion treatment using bath containing chromium salt is widely used on many alloys to protect them against corrosion. However, European environmental standards have considerably restricted the use of hexavalent chromium baths because of its high toxicity [1, 2].

Recently, research has shown that the use of less toxic and more eco-friendly elements, such as, rare earth can be a good strategy to replace chromate. Generally, the rare earths are in low concentration with specific ratios in a variety of ores; cerium and yttrium are the most commonly detected elements.

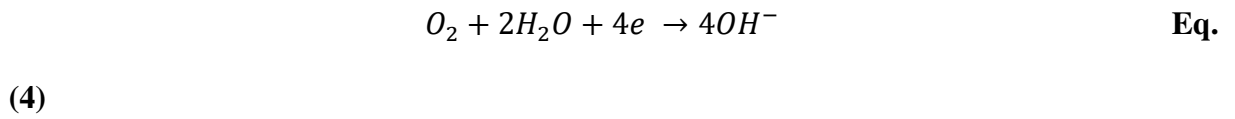
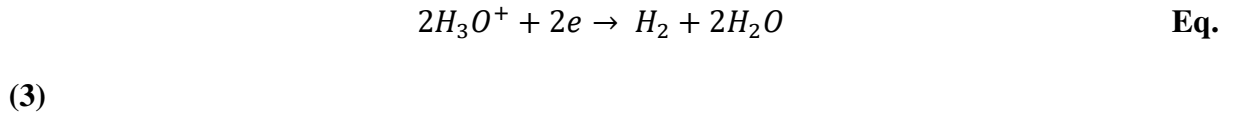
Cerium-based oxide coating are one of the most promising technology for surface modification and corrosion protection of many metal substrates: aluminium [3-7], steel [8-11], stainless steel [12-14], magnesium containing alloys [15-17], galvanized steel [18-23] or zinc [24-30]. Interest in cerium oxides increased significantly in recent decades due to promising features such as being environmentally friendly, increasing the adhesion strength of some coatings to the substrate and improving corrosion protection performance.

Among the various techniques used to obtain a ceria (CeO_2) deposit, cathodic electrodeposition is the most attractive method [5-7, 9, 10, 14, 22, 30] since it offers the advantage of low processing temperature, controlled thickness of the film and low cost process. Hamlaoui et al. [7], Poupard et al. [22], Arurault et al. [31] have used a solution of Ce (III) nitrate in order to deposit thin oxide films. The method is based on the reduction of dissolved oxygen and nitrate ions to generate OH^- ions, inducing an interfacial pH increase at the electrode surface. The pH increase favors the precipitation of cerium hydroxide, as represented in the following reactions [31]:

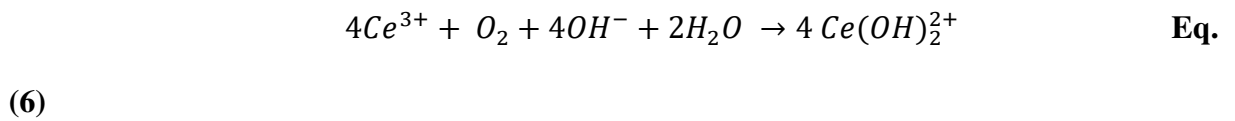
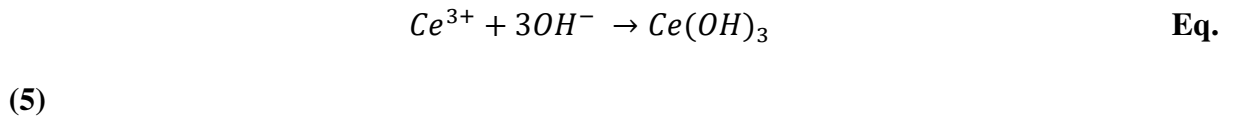
Nitrate ions could be reduced into nitrite and/or ammonium ions:



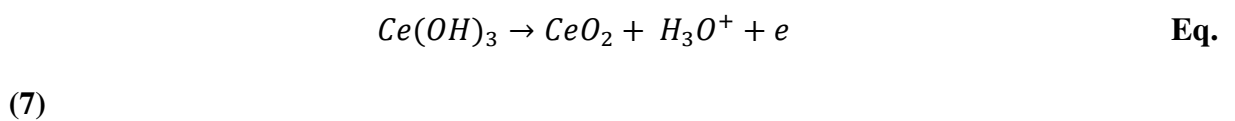
Furthermore, H_3O^+ ions and dissolved O_2 may also be reduced simultaneously by the following reactions:

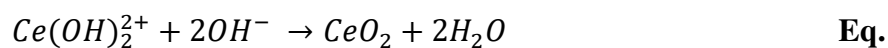


The consumption of H_3O^+ ions in reaction **Eq. (3)** as well as the formation of OH^- ions in reactions **Eq. (1, 2, 4)** at the cathode lead to an interfacial pH increase, which induce the precipitation of cerium hydroxide $Ce(OH)_3$ following the reaction **Eq. (5)**, and/or the formation of the soluble ionic complexes such as $Ce(OH)_2^{2+}$ **Eq. (6)**. However, this latter reaction is less probable from a kinetic point of view, as it involves a large number of species, but it is not excluded.



Then, CeO_2 should result from oxidation during the increase of the pH of the solution and/or dehydration of the electrodeposited compounds following reactions **Eq. (7 and 8)**:





(8)

However, cerium oxide coating (CeO_2) did not exhibit high corrosion resistance due to its non-compact morphology and highly porous and cracked microstructure, giving rise to the preferential pathways for the attack of the underlying substrate and thus accelerating the coating degradation. These defects limit their use as a protective coating in corrosive media, such as seawater. It is necessary to improve the morphology and microstructure of the traditional CeO_2 coating to obtain better corrosion resistance.

In recent years, various studies have been devoted to improving the corrosion protection properties of cerium-based coatings on steel substrates. Kobayashi et al. [32] have studied the effect of addition of sulphate ions on the corrosion resistance of CeCC on galvanized steel. The results show that the presence of sulphate in the conversion bath leads to a significant improvement of corrosion resistance of cerium coating; this being attributed to its fine and dense grain structure covering the entire surface of the metal. Ramezanzadeh et al. [33] used zinc phosphate conversion coating as a sealing agent in order to improve the anticorrosive performances of CeCC sub-layer. The results reveal that the post-treatment of cerium based coatings by zinc phosphate coating leads to a more compact coating with less cracks and better corrosion resistance. Another study, Parhizkar et al. [34] nano-sheets of graphene oxide covalently functionalized with a silane coupling agent (AGO), were used to modify the conversion coating to cerium and its effect on cathodic disbanding, corrosion protection and adhesion properties of epoxy coating on steel. The results reveal that the addition of AGO nano-sheets to the cerium conversion coating led to the better adhesion strength and thus increasing the corrosion resistance of the steel. The cathodic delamination rate of epoxy coating was also reduced.

Recently, Brucite $\text{Mg}(\text{OH})_2$ has shown strong interest in various applications, including in the corrosion protection application, because of its non-toxicity properties and low cost [35]. It is widely used in surface treatment for Mg alloys to enhance its corrosion resistance. Guo et al. [36] have synthesized a $\text{Mg}(\text{OH})_2$ hydrothermal conversion coating on a Mg-2Zn-Mn-Ca-Ce biomedical Mg alloy. They have showed that the coatings were macroscopically uniform and compact and provided an effective protection against corrosion of Mg alloy in Hanks' solution. Another study, Jeong et al. [37] also reported improving the corrosion resistance in NaCl medium of film de $\text{Mg}(\text{OH})_2$ deposited on AZ31 magnesium alloy using an alkaline hydrothermal method.

Our interest in this work is focused on using magnesium hydroxide to improve the corrosion protection properties of cerium-based oxide coating. For that, mixed layer of cerium oxide and magnesium hydroxide ($\text{Mg}(\text{OH})_2/\text{CeO}_2$) were deposited onto low alloyed steel in order to improve its resistance against marine corrosion. First, CeO_2 coating was formed on steel substrate by cathodic electrodeposition in a low concentration of cerium nitrate bath. Then, $\text{Mg}(\text{OH})_2$ layer was deposited on the surface and the micro-pores/micro-cracks of these obtained oxide layer. Precipitation of brucite in the ceria defects seems to provide high corrosion protection for the composite coatings. So the formation of a composite coating is an innovating method that permits to enhance the corrosion resistance of ceria based conversion coatings on steel substrate for marine applications.

2. Experimental

2.1. Preparation of steel substrate

AISI 4135 steel (whose composition determined by optical emission spectrometry are reported in table 1) was used for this study. The samples were first cut into cylindrical coupons with 2mm thick and 7cm^2 of surface area, and then enrobed in an epoxy resin. The samples were grinded by emery paper 180, 320 and 600 SiC grades, followed by rinsing with

ethanol then ultrapure water and finally dried with pulsed air immediately before the deposition of the film.

2.2.Synthesis of the Mg(OH)₂/CeO₂ mixed coating

The elaboration of Mg(OH)₂/CeO₂ based deposit coating on steel requires two steps. Firstly, CeO₂ coating formed on steel in galvanostatic condition -1mA/cm² during 30min in a stirred electrolytic bath of 0.05M Ce(NO₃)₃, 6H₂O and 0.6M KNO₃ (pH=4.2). The addition of nitrate potassium aims to maintain a good conductivity of the solution and thus to increase the kinetics of deposition by favoring nitrate reduction. The electrochemical experiments were performed using standard three electrodes chemical cell. The working electrode was the prepared steel. The counter electrode was a large platinum grid and all potentials were recorded with respect to a saturated calomel electrode (SCE). After deposition, CeO₂ coated steels were directly rinsed with ultrapure water and dried with hot air.

After that, a magnesium hydroxide was formed on the ceria coating in stirred bath of 0.1M Mg(NO₃)₂, 6H₂O. The solution pH was adjusted at 8.3 with 0.1M NaOH solution. Two cathodic potential were imposed, -1 and -1.1V/SCE during 24h. The electrochemical experiments were carried out in an electrochemical cell with a KNO₃-based salt bridge in a U-shaped tube **Fig. (1)** in order to avoid acidification of deposition bath by oxidation reactions occurring at the anode (counter electrode). Finally, samples were rinsed with distilled water and then dried with pulsed air. Coated samples were conserved in desiccators before any further subsequent analysis. All the experiments were performed at room temperature with Biologic VSP, driving by EC-Lab software.

2.3.Surface characterization of coatings

Microstructures of coatings deposited on steel (surfaces and cross sections) were analyzed by Scanning Electronic Microscopy (Quanta SEM Philips) equipped with an Energy Dispersive X-ray Spectroscopy (EDS). The structure of coatings was obtained by an X-ray diffractometer

(XRD, Bruker AXS D8- Advanced diffractometer) with Cu-K α 1 wavelength ($\lambda = 1.5406$ nm) at a scanning rate of $0.04^\circ/6s$ in the 2θ range of $5^\circ \sim 70^\circ$. The coatings were also analyzed using both a LabRam HR and a LabRam HR Evo spectrometer from Horiba-Jobin Yvon, equipped with a confocal microscope, using an incident beam of 632.82 and 533 nm emitted by an HeNe laser and laser diode respectively. As a 50X long working distance objective was used, each spectrum corresponds to a surface of $2 \times 2 \mu\text{m}$ analyzed. For each point, an acquisition of $2 \times 60s$ in the low frequencies range (100 to 1300 cm^{-1}) and $2 \times 30s$ in the high frequencies range (3400 to 3800 cm^{-1}) were performed.

2.4. Electrochemical corrosion evolution

The protection efficiency of synthesized coatings was studied and compared with bare steel for six days of immersion in 2L of stirred artificial seawater solution (ASTM standard D1141). The open circuit potential (OCP) was recorded during the entire immersion period. The linear polarisation resistance (LPR) measurements were carried out at a scan rate of 0.2 mV/s about $\pm 20 \text{ mV/OCP}$. Then polarisation curves were obtained after 1 and 6 days of seawater immersion on different samples of CeO_2 coating and $\text{Mg(OH)}_2/\text{CeO}_2$ mixed coating at a scan rate of 10 mV/s . In order to avoid modifications of the surface due to the polarisation and to test the **reproducibility**, corrosion tests for each deposit were performed 2 times.

A cathodic polarisation was carried out on the samples from OCP to -2 V/OCP . On the other hand, anodic polarisation on other samples from OCP to $+2 \text{ V/OCP}$. The cathodic and anodic curves were combined at OCP to obtain a full polarization curve.

3. Results and discussion

3.1. Characterisation of Cerium oxide Coating

After electrodeposition of the cerium oxide based coating on steel, SEM observations on the surface (a) and cross-section (b) illustrated in **Fig. (2)** reveal that the thickness of the coating is about $26 \mu\text{m}$; its morphology is typically the same as those described in the literature [5, 6,

8, 10, 22, 30, 31]. The deposit has a needle-like microstructure, characterized by a large network of cracks. The average width of cracks measured at the surface of coating is about 1.2 μm (± 0.2). However, the cross section image reveals that these micro-cracks are non-crossing. The formation of the cracks is associated to different process: the hydrogen bubble released during the electrodeposition process, the dehydration process itself [9] or from the shearing stress between the substrate and the deposit [31]. The cracks area determined on the coating surface by ImageJ software is about 2.38 %.

The Raman Spectroscopy measurement of the coating surface is presented in **Fig. (3.a)**. The spectrum exhibits an intense peak at about 456 cm^{-1} attributed to the F_{2g} triply degenerate mode of CeO_2 fluorite structure [38-40], which originates from the symmetric vibrations of oxygen atoms around the Ce^{4+} . It is highly sensitive to oxygen related disorder [41]. Hence, any changes in the Ce ionic state or the oxygen lattice strongly affect this vibration mode. The broadening of this peak indicates the formation of a nano-crystalline phase of ceria. While its strong asymmetry and the presence of broad and weak peak at around 600 cm^{-1} are attributed to oxygen vacancies due to Ce^{3+} ions resulting from the reduction of Ce^{4+} [42, 43]. This suggests the formation of a non-stoichiometric oxide layer CeO_{2-x} . Some studies show that the concentration of Ce^{3+} increases as the crystallite size decreases [44, 45].

Peaks located at 1048 and 740 cm^{-1} correspond to the N-O bonds vibration of the nitrate group [46] incorporated in the cerium oxide film [10]. The presence of nitrate is a consequence of a fast growth process [30], but it may also be related to the compensation of charges in the non-stoichiometric oxide layer.

The XRD pattern of the coating is shown in **Fig. (3.b)**. As can be seen, the diffractogram confirm the composition of the coating, it also presents the characteristic peaks of cerium oxide (CeO_2), which are attributed to ceria. The main diffraction peaks of the oxide located at $2\theta = 28.5^\circ, 33^\circ, 47.4^\circ, 56.3^\circ, 59^\circ$ correspond respectively to the (1 1 1), (2 0 0), (2 2 0), (3 1 1), (2 2 2) crystallographic planes of the cubic ceria crystal structure (referring to JCPDS file

N°. 34-0394). The broadening of the peaks suggests a nanostructured oxide film composed of tiny crystallites. Indeed, the crystallite size is found lower than 4nm. This was calculated for (111) plane of CeO₂ using Scherrer's relation by taking into account the diffractometer broadening. XRD pattern exhibits also two peaks at 2θ= 44.6°, 65° attributed to the α-Fe substrate (referring to JCPDS file N°. 65-4899).

3.2. Magnesium hydroxide deposition on cerium oxide coating

In this part, Mg(OH)₂ layer was formed on CeO₂ coating in order to seal the cracks and other porosities of the oxide film. This layer was prepared under potentiostatic polarisation at -1 and -1.1V/SCE during 24h in a magnesium nitrate solution. Fig. (4) shows the evolution with time of the normalised current densities recorded during the formation of the Mg(OH)₂ deposit on CeO₂ coating for both applied potentials. The curves follow a similar behavior whatever the applied potential. There were characterised by a drop of the current followed by a pseudo stability.

The sharp decrease of the current indicates a reduction of the active surface where nitrate Eq. (1 and 2), oxygen Eq. (4) and water Eq. (9) reduction take place. Due to a solubility product constant $K_S=[Mg^{2+}]_{eq} [OH^-]_{eq}^2 = 2.4 \cdot 10^{-11} \text{ mol}^2/\text{L}$, the resulting interfacial pH increase gives rise to the precipitation of brucite following Eq. (10) [47].



(9)



(10)

Whatever the applied potential, the curves display a significant decay of the reduction current following by a current plateau at about 82-84% of the initial current. These values of I/I_0 are comparable to those obtained by Ch. Barchiche and al. [48] on the deposition on carbon steel of a Mg(OH)₂ layer in artificial seawater free of Ca²⁺ ions. About 20% of the steel surface remains active due to the porous and gel-like nature of the Mg(OH)₂ layer. Hydrogen bubbles

that are formed due to the water reduction **Eq. (9)** also influence the porosity. Indeed, hydrogen evolution start on carbon steel at about -1.0 V/SCE [48] and the fluctuation of current observed in **Fig. (4)** during the fast decrease should correspond to hydrogen bubbles that release through the deposit.

Fig. (5) shows the SEM images obtained on the surface of coatings synthesized at both applied potentials. Both surface exhibits cracks network with a lowest density compare to the ones observed on a pure CeO₂ deposit. Indeed, the cracks areas determined by ImageJ software is 0.62 and 0.34% for mixed coatings obtained at -1V and -1.1V/SCE respectively.

Coatings have a fibrous structure made of hexagonal platelets characteristic of brucite. The coating performed at higher applied potential seems to be more compact. Surface of both coatings presents some defects localised on the surface. We observe the agglomeration of platelets with no particular shape that are scattered on all surface of coatings. The chemical composition of these agglomerates are the same as the net surface of the coatings, with a slightly higher percentage of cerium. The EDS quantification performed on these agglomerates on both coatings shows that the percentage of cerium is higher in the case of the coating obtained at lower applied potential. These specific points could be the places where hydrogen bubbles are released from the steel interface, bringing with it CeO₂ particles that mixed with brucite layer.

The XRD analyses illustrated in **Fig. (6)** reveal that the coatings were essentially composed of brucite Mg(OH)₂. All the peaks obtained show that the both deposits have a well crystalized structure. The diffractograms present characteristic peaks of brucite located at $2\theta = 18.6^\circ$, 32.8° , 38° , 50.8° , 58.5° , 62° , 68.2° corresponding respectively to the (0 0 1), (1 0 0), (0 1 1), (0 1 2), (1 1 0), (1 1 1), (0 1 3) crystallographic planes of the hexagonal crystal (referring to JCPDS file N°. 71-5972). Average size crystallites calculated by the Scherrer equation for the both deposits is about 20nm. Trace of CeO₂ is only visible on the coating synthesized at -1 V/SCE by its peak at $2\theta = 28.5^\circ$. As deposit thicknesses are the same, whatever the applied

potential (see SEM analysis below), the detection of CeO₂ at the surface is likely due to the spherical agglomerates that are more noticeable on coating obtained at -1 V/SCE.

The cross sections of these mixed coatings were also observed by scanning electronic microscopy. Their morphologies are illustrated in **Fig. (7)**. The thickness of the bilayer coatings are almost equal, i.e. 148 and 150 μm for -1 and -1.1V/SCE applied potential respectively.

These cross-section pictures confirm that the mixed coating formed at -1.1 V/SCE exhibits more uniform structure with less cracks than the coating formed at -1 V/SCE. Nevertheless, cracks are larger (5.3 ±0.7 μm) than the ones obtained at -1 V/SCE (2.4 ±0.5 μm). For both samples, these cracks are crossing the entire mixed coating and should result from the H₂ bubbles that release from the steel due to water reduction.

According to these SEM images, the cross-sections feature of the coatings can be described as a bi-layered structure. As revealed by EDS analyses **Fig. (8)**, the internal layer (light grey) is mainly composed of cerium and oxygen, corresponding to the previous Ce₂O layer. Mg is also detected with a concentration that increases as we move away from the steel surface. As revealed by μ-Raman spectroscopy of this cross-section, Mg is found in Brucite form inside the Ce oxide (see **Fig. (9)**). Indeed, Raman spectrum obtained on the underneath layer of coating **Fig. (9.a)** exhibits an intense band at 455 cm⁻¹ corresponding to the vibrational mode of cerium oxide (CeO₂). Whereas the presence of brucite is revealed by peaks at 280 and 444 cm⁻¹ in the low wavenumber range and an intense peak at 3654 cm⁻¹ in the high wavenumber range corresponding to the O-H stretching vibration of the hydroxyl group [49]. This result confirms the incorporation of the brucite inside the CeO₂ structure. Concerning the upper dark-grey layer of **Fig. (7.b)**, it is composed of Mg and O as revealed by EDS analysis **Fig. (8)** that corresponds to brucite revealed by Raman analysis (see **Fig. (9.b)**). This spectrum shows also the presence of nitrate (vibration bands at 740 and 1048 cm⁻¹) incorporated into the Mg(OH)₂ film.

3.3. Electrochemical corrosion evaluation of coatings

In order to evaluate the contribution of $\text{Mg}(\text{OH})_2$ layer to corrosion resistance of CeO_2 coating, the corrosion tests were carried out during 6 days of immersion in artificial seawater (ASTM D1141 standard) on the bare steel, CeO_2 coating and the composite coating : $\text{Mg}(\text{OH})_2 / \text{CeO}_2$ for which the synthesis of brucite was performed at -1.1V/SCE .

3.3.1. Open circuit potential evolution and polarization experiments

The OCP evolutions of bare steel, CeO_2 coating and $\text{Mg}(\text{OH})_2/\text{CeO}_2$ mixed coating were recorded for 6 days of immersion. They are presented in **Fig. (10.a)**. We first notice that initial potentials of both coated steels are slightly less negative than for bare steel. This ennoblement of the OCP is due to the presence of the mixed film that limit the access to the electrolyte. We observe a shift of OCP to nobler values due to the coatings. Bare steel remains at -700 mV/SCE corresponding to OCP value of carbon steel in seawater [50] giving rise to a generalized corrosion process. $\text{CeO}_2/\text{steel}$ sample exhibit an OCP slightly nobler at -650 mV/SCE . The corrosion of the substrate is then localized at the open defects (porosities and open cracks) of the ceria-based film. The presence of residual nitrate ions inside the ceria layer may accelerate the substrate degradation through the open defects and may favors the formation of corrosion layer. Ceria based coating seems to be not able to bring a long-term protection of the steel substrate in marine solution due to the presence of open defects. It is important to develop a technic that will be able to seal these open defects and/or perhaps to bring an active protection that modify the corrosion behavior during the exposure to marine environment. That is the reason why a magnesium hydroxide film was cathodically deposited on the surface of the ceria based films.

For mixed coating, OCP decreases very slowly during the immersion and stabilizes at around -600 mV/SCE after 70h of immersion. The infiltration of the electrolyte through the mixed coating seems to be reduced, provoking a delay in the decrease of the OCP values. The OCP

seems to stabilize at highest values, suggesting that the mixed coating present a reinforced corrosion protection compared to the CeO₂ coating.

These results are confirmed by potentiodynamic polarization experiments performed after 6 days of immersion **Fig. (10.b)**. Even these experiments were performed at a high scan rate (10 mV/s) compare to conventional low scan rate used for this kind of experiment, we can clearly show the effects of coatings on the anodic and cathodic reactions especially in the case of the mixed coating. A slight decrease of the anodic branch due to the deposit is observed. This branch is flattened due to the slowdown of the infiltration path of the electrolyte toward the substrate and perhaps due to an active protection ensured by the presence of brucite film. At the same time the cathodic branch is also strongly decreased in the case of mixed coating. The deposit inhibits the oxygen diffusion and thus reduces the cathodic current. The mixed coating acts both on anodic and cathodic reaction. The deposition of brucite improved the corrosion resistance of the ceria based coating deposited onto steel, decreasing both the cathodic and anodic activity of the sample.

3.3.2. Polarisation resistance measurements (Rp)

The **Fig. (11.a)** presents the results of polarisation resistance measurements of bare steel, CeO₂ coating and Mg(OH)₂/CeO₂ mixed coating as a function of immersion time in artificial seawater. These measurements show that the both coatings improve the Rp of steel, in particular the mixed coating. We notice that the Rp values of the mixed coating remain higher than CeO₂ coating during the entire period of immersion, which indicates that it has a better resistance to corrosion.

The curve $R_p=f(t)$ corresponding to the CeO₂ coating remains almost constant at about 1.7 kΩ.cm² during the immersion and is 1.7 time higher than Rp of bare steel (about 1 kΩ.cm²). This coincides with OCP evolution registered on this coating and the reduction of the steel dissolution observed by polarization measurements **Fig. (10.b)**. Unfortunately the corrosion

of the steel occurs rapidly through the open defects and the steel corrosion product are spread over the entire surface of the sample, as observed on picture of the surface after 6 days of immersion (see picture in **Fig. (11.b)**). The white CeO₂ coating is no more observed and orange and black corrosion products are covering the entire surface.

The mixed coating exhibits a decrease of R_p during the first hours of immersion. It is mainly due to the infiltration of the electrolyte through the residual open defects of the coating and the large cracks of the deposit observed (see **Fig. (7.b)**). Anyway, it should be noticed that the initial polarisation resistance of the mixed coating is superior to 4 kΩ.cm², suggesting that the brucite film has a beneficial effect provoking a partial sealing of the ceria film. Nevertheless, open defects and large cracks are still present, explaining the progressive decreases of the R_p up to 30h of immersion and its stabilization at around 2 kΩ.cm². A local degradation of the steel surface is possible through the open defects, provoking the decrease of the R_p value and perhaps the modification of the local chemistry composition of the solution inside the defects. After 40h of immersion, the R_p strongly and continuously increases during the immersion period up to about 19 kΩ.cm², about 20 times higher than the bare steel. The corrosion resistance is then strongly improved by the mixed coating. It is confirmed by pictures of the immersed sample before and after corrosion experiments **Fig. (11.b)**. No evidence of corrosion product is seen on the Mg(OH)₂/CeO₂ mixed coating after 6 days of immersion in seawater whereas steel corrosion products completely spread over the entire surface of the CeO₂ coated steel.

The electrochemical measurements combined with the optical observations of the immersed samples after 6 days of immersion confirmed that the mixed coating presents the highest corrosion resistance. The important increase of the thickness at about 130μm and the partial sealing of the ceria underlayer permits to limit the infiltration of the electrolyte through the coating, but the barrier effect or passive protection is not as good as expected due to the specific defects induced by the deposition process (larges cracks). The specific interest of our

mixed coating is that brucite seems to bring not only a passive protection, reinforcing the barrier effect of the ceria film but also an active protection that permits to limit the steel degradation as observed by the optical pictures after 6 days of immersion.

3.4. Characterisation of coatings after seawater immersion

In order to understand the effect of the brucite layer on the protective mechanism of CeO₂ coating against marine corrosion of steel, the surfaces of both coatings after seawater immersion were analysed by XRD. The cross sections of these coatings were observed by SEM, and analysed by EDS cartography and μ -Raman spectroscopy.

The XRD patterns of both coatings after seawater immersion are presented in **Fig. (12)**. the diffractogram of CeO₂ coating **Fig. (12.a)** shows the characteristic peaks of Lepidocrocite located at $2\theta = 14.1^\circ; 27^\circ; 36.2^\circ; 38^\circ; 46.9^\circ; 49.2^\circ; 52.7^\circ; 60.1^\circ; 60.7^\circ$ (referring to JCPDS file N° 70-8045), Aragonite at $2\theta = 21^\circ; 26.2^\circ; 33.1^\circ; 37.2^\circ; 41.2^\circ; 42.9^\circ; 45.8^\circ; 48.3^\circ; 50.2^\circ; 59.2^\circ; 68.6^\circ$ (referring to JCPDS file N° 70-9854) and Iron at $2\theta = 44.6^\circ, 65^\circ$ (referring to JCPDS file N° 65-4899). Aragonite is one of the allotropic form of CaCO₃ that compose the calcareous deposit that could be formed in seawater and it appears preferentially on the cathodic sites where a pH increase is produced. No diffraction peaks of cerium oxide were detected while the coating remains present in some area of the sample after 6 days of immersion. In fact, EDS analyses and μ -Raman spectroscopy (spectra not shown) of the cross-section show zones remaining covered by CeO₂ layer (see **Fig. (13.a)**), but the major part of the surface is mainly degraded and covered by a thick corrosion layer made of lepidocrocite **Fig. (13.b)**. These analyses confirms that steel corrosion occurs at the open defects of the ceria film. The presence of nitrate ions incorporated during the ceria formation promotes and accelerates the steel degradation that progressively leads to an important delamination.

The diffractogram pattern obtained on the mixed coating **Fig. (12.b)** shows only characteristic peaks of Aragonite. It reveals that the surface of the mixed coating is completely covered by a

thick aragonite layer formed during **the** seawater immersion **that** explains the strong cathodic current decrease observed on **the** polarization curve **obtained after 6 days of immersion** **Fig. (10.b)**.

This coating is in fact more complex as revealed by the cross section observed by SEM **Fig. (14.a)**. The mixed coating is now composed of three different layers. The internal layer in contact to the steel correspond to **the** Ce rich layer **whose characteristics and thickness do not change**. **The intermediate layer is mainly composed of brucite**. The thickness of the brucite layer has **considerably** decreased and a new deposit has formed on top as well as inside the **large** cracks of **the mixed** coating.

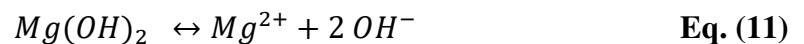
The EDS cartography of this cross section **Fig. (14.b)** shows that calcium from aragonite that compose the external layer is also detected inside the **large** cracks **up to** the steel surface. **The SEM observations confirm that the** intermediate layer is mainly composed of magnesium whereas the internal layer is composed of Cerium. μ -Raman analyses of the cross-section **Fig. (15)** confirm that the external layer is composed of aragonite. The Raman spectrum **Fig. (15.a)** presents an intense peak at 1085 cm^{-1} corresponding to the symmetric vibration mode of CO_3^{2-} and small peaks at 155; 205 and 704 cm^{-1} characteristic of aragonite [51]. The intermediate layer correspond to the previously formed brucite layer **Fig. (15.b)**. The internal layer is made of cerium oxide containing brucite **Fig. (15.c)** as observed before corrosion tests. The main difference is the presence of aragonite inside the internal layer (see small vibration band at 1085 cm^{-1} in **Fig. (15.c)**) and in all the deposit cracks. Indeed, cracks are totally filled by aragonite (see Raman cartography below).

In order to evaluate the aragonite distribution inside the mixed coating after seawater immersion, μ -Raman cartography was performed on the same cross section as observed by SEM. This cartography was performed by point-by-point acquisition mode on a surface of $25 \times 222\text{ }\mu\text{m}$ containing the crack (**see picture Fig. (17.a)**). A $1.7\text{ }\mu\text{m}$ step in the x direction and a $7.14\text{ }\mu\text{m}$ step in the y direction were chosen. So, each pixel corresponds to a surface of 12

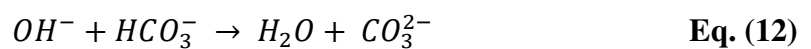
μm^2 whereas each spectrum to an analysed surface of about $4 \mu\text{m}^2$. The intensity of each pixel is then proportional to the vibration bands area characteristic of each compound (peaks at 1086 cm^{-1} for aragonite, 457 cm^{-1} for CeO_2 and 3654 cm^{-1} for brucite – see **Fig. (16.a)**). But as CeO_2 vibration band at 457 cm^{-1} overlaps the band at 446 cm^{-1} of brucite, a Gaussian deconvolution was performed (see in **Fig. (16.b)**) in order to extract the band of ceria. The accuracy of the deconvolution was checked by comparing the cartography of brucite obtained by the vibration band at 3654 cm^{-1} to the one obtained at 447 cm^{-1} (image not shown).

The **Fig. (17.a)** present an optical microscope view of the analysed area of the cross section. **Fig. (17. b,c,d)** show the spatial distribution of the different compounds such as aragonite, brucite and cerium oxide. These results show that brucite is well incorporated inside the cerium oxide layer (presence of grey spots between $y=125$ and $150 \mu\text{m}$ corresponding to the ceria layer) and that aragonite, not only filled the crack but is also detected in both brucite and ceria layer around the crack.

The precipitation of aragonite above and inside the crack of the mixed coatings is due to the brucite layer. This is related to the partial dissolution of the $\text{Mg}(\text{OH})_2$ layer as it was demonstrated by Nguyen et al. [52]. It then releases hydroxyl ions that increase the local pH and then favor the formation of calcium carbonate CaCO_3 . Due to the presence of Mg^{2+} ions, it is the aragonite form which precipitates. The pH of precipitation of $\text{Mg}(\text{OH})_2$ being around 9.3, in contact with seawater at $\text{pH}=8.2$, brucite start to dissolve according to the reaction **Eq. (11)**,



and produce a pH increase that induces an equilibrium shift between the hydrogenocarbonate and carbonate ions in seawater following the reaction **Eq. (12)** [47, 52].



which gives rise to the CaCO_3 précipitation **Eq. (13)** as soon as the solubility product **Eq. (14)** is reached.



$$K_S = [Ca^{2+}]_{eq} [CO_3^{2-}]_{eq} = 9.42 \cdot 10^{-7} \text{ mol}^2/\text{L} \quad \text{Eq. (14)}$$

This $CaCO_3$ layer reinforces the mixed coating and creates a physical barrier against oxygen diffusion and various chemical species present in seawater to reach the surface of the substrate.

During the immersion, we observe that the R_p decreased during the first hours of immersion, resulting from the local degradation of the steel through the open defects, but this degradation seems to locally emphasize the dissolution of the $Mg(OH)_2$ that was initially present in the defects. The pH increase favours the precipitation of stable oxide resulting from the steel degradation and also the precipitation of the calcium carbonate.

Furthermore, we observe a strong decrease of the cathodic branch as well as the anodic reaction after 6 days of immersion and then, a strong increase of R_p for the $Mg(OH)_2/CeO_2$ mixed coating due to the reinforcement of the barrier properties of the mixed films. These mixed films combine a passive protection linked to their barrier effect and an active protection that permit to enhance and/or reinforce the passive protection.

4. Conclusion

In the present study, $Mg(OH)_2$ layer was formed on CeO_2 coated steel in order to enhance its marine corrosion resistance. The characteristics of the coatings were confirmed via SEM, XRD and μ -Raman analyses. The porous and cracked microstructure of CeO_2 coating resulted allowed the corrosive species to reach the steel surface. Consequently, this layer did not provide a strong protection to steel against marine corrosion.

On the other hand, $Mg(OH)_2/CeO_2$ mixed coatings have uniform and compact microstructure. We conclude that the morphology and structure of the mixed coatings depend on the applied potential. The coating deposited at high potential presents a more compact structure and a low cracks network. These cracks are larger because of hydrogen release during the cathodic

polarization and presence of internal stress. However, brucite was found interlace with the CeO₂ layer.

The corrosion tests reveal that the brucite layer offers to CeO₂ coating by its partial dissolution a significant improvement of marine corrosion resistance. The partial Brucite dissolution has a double effect. On the one hand, it favor the precipitation of CaCO₃ above and inside cracks that acts as an effective barrier. On the other hand, by increasing the internal pH, it favors the formation of a more stable oxide layer combined with calcium carbonate and the steel dissolution is strongly reduced. The polarization resistance of mixed coating increases significantly throughout the seawater immersion, whereas the polarisation resistance of ceria coating remains inconsiderable.

Mg(OH)₂/CeO₂ mixed coatings seems to be a good protection technique of steel against marine corrosion. These coatings combine a passive and active protection. Moreover, it is eco-friendly because a part of the mixed coating is made with magnesium that is naturally present in seawater. Despite the partial dissolution of brucite layer associated to the active protection of the mixed layer, we can underline that it is possible to regenerate the brucite layer in seawater by a simple cathodic polarisation.

Acknowledgments:

This study was granted by the French and Algerian governments through a Hubert Curien Program- PHC Tassili and by PROFAS B+ grant from the Algerian government.

References:

1. Åslund, J., *Release rates and environmental impact of zinc-nickel coatings in the automotive industry*. 2006. p. vii, 75.
2. *Directive 2000/53/CE*. 2000.
3. Yu, X. and G. Li, *XPS study of cerium conversion coating on the anodized 2024 aluminum alloy*. *Journal of Alloys and Compounds*, 2004. **364**(1): p. 193-198.

4. Fahrenholtz, W.G., et al., *Characterization of cerium-based conversion coatings for corrosion protection of aluminum alloys*. *Surface and Coatings Technology*, 2002. **155**(2): p. 208-213.
5. Tang, J., et al., *A corrosion resistant cerium oxide based coating on aluminum alloy 2024 prepared by brush plating*. *Applied Surface Science*. Vol. 257. 2011. 2806-2812.
6. Živković, L.S., et al., *Corrosion study of ceria coatings on AA6060 aluminum alloy obtained by cathodic electrodeposition: Effect of deposition potential*. *Surface and Coatings Technology*, 2014. **240**: p. 327-335.
7. Hamlaoui, Y., et al., *Cathodic electrodeposition of cerium-based oxides on carbon steel from concentrated cerium nitrate solutions: Part I. Electrochemical and analytical characterisation*. *Materials Chemistry and Physics*. Vol. 113. 2009. 650–657.
8. Avramova, I., et al., *Characterization of nanocomposite CeO₂–Al₂O₃ coatings electrodeposited on stainless steel*. *Composites Science and Technology*, 2005. **65**(11): p. 1663-1667.
9. Creus, J., et al., *Synthesis and characterisation of thin cerium oxide coatings elaborated by cathodic electrolytic deposition on steel substrate*. *Surface and Coatings Technology*, 2006. **200**(14): p. 4636-4645.
10. Poupard, S., F. Pedraza, and J. Creus, *Synthesis and characterisation of thin cerium-based oxide films by celd on zinc metal*. *Advances in Materials Science*. Vol. 7. 2007.
11. Hamlaoui, Y., F. Pedraza, and L. Tifouti, *Corrosion monitoring of galvanised coatings through electrochemical impedance spectroscopy*. *Corrosion Science*, 2008. **50**(6): p. 1558-1566.
12. Virtanen, S., et al., *A surface analytical and electrochemical study on the role of cerium in the chemical surface treatment of stainless steels*. *Corrosion Science*. Vol. 39. 1997. 1897-1913.
13. Golden, T. and Q. Wang, *Anodic Electrodeposition of Cerium Oxide Thin Films II. Mechanism Studies*. *Journal of The Electrochemical Society*. Vol. 150. 2003.
14. Stoychev, D., *Corrosion protective ability of electrodeposited ceria layers*. *Journal of Solid State Electrochemistry*. Vol. 17. 2012.
15. Arenas, M.A., A. Conde, and J.J. de Damborenea, *Cerium: a suitable green corrosion inhibitor for tinplate*. *Corrosion Science*, 2002. **44**(3): p. 511-520.
16. Liu, H.-T., et al., *Effect of cerium on the anodic corrosion of Pb–Ca–Sn alloy in sulfuric acid solution*. *Journal of Power Sources*. Vol. 93. 2001. 230-233.

17. Lei, L., et al., *Surface characterization of growth process for cerium conversion coating on magnesium alloy and its anticorrosion mechanism.* **Surface and Interface Analysis.** Vol. 46. 2014.
18. Montemor, M., A. Simões, and M. Ferreira, *Composition and behaviour of cerium films on galvanised steel.* **Progress in Organic Coatings.** Vol. 43. 2001. 274-281.
19. Arenas, M.A. and J.J. de Damborenea, *Growth mechanisms of cerium layers on galvanised steel.* *Electrochimica Acta*, 2003. **48**(24): p. 3693-3698.
20. Ferreira, M.G.S., et al., *Silanes and rare earth salts as chromate replacers for pre-treatments on galvanised steel.* *Electrochimica Acta*, 2004. **49**(17): p. 2927-2935.
21. Motte, C., et al., *Cerium treatments for temporary protection of electroplated steel.* **Surface & Coatings Technology.** Vol. 200. 2005. 2366-2375.
22. Poupard, S., F. Pedraza, and J. Creus, *Diffusion of a Corroding Electrolyte through Defective Electroplated Ceria Based Coatings.* **Defect and Diffusion Forum.** Vol. 289-292. 2009. 235-242.
23. Deflorian, F., et al., *Evaluation of mechanically treated cerium (IV) oxides as corrosion inhibitors for galvanized steel.* **Electrochimica Acta.** Vol. 56. 2011. 7833-7844.
24. Aramaki, K., *Treatment of zinc surface with cerium(III) nitrate to prevent zinc corrosion in aerated 0.5 M NaCl.* **Corrosion Science.** Vol. 43. 2001. 2201-2215.
25. Aramaki, K., *Self-healing protective films prepared on zinc electrodes by treatment in a cerium(III) nitrate solution and modification with sodium phosphate and calcium or magnesium nitrate.* **Corrosion Science.** Vol. 45. 2003. 2361-2376.
26. Aramaki, K., *A self-healing protective film prepared on zinc by treatment in a Ce(NO₃)₃ solution and modification with Ce(NO₃)₃.* **Corrosion Science.** Vol. 47. 2005. 1285-1298.
27. Aramaki, K., *The effect of modification with hydrogen peroxide on a hydrated cerium(III) oxide layer for protection of zinc against corrosion in 0.5 M NaCl.* **Corrosion Science.** Vol. 48. 2006. 766-782.
28. Aramaki, K., *Prevention of zinc corrosion in oxygenated 0.5 M NaCl by treatment in a cerium(III) nitrate solution and modification with sodium hexadecanoate.* **Corrosion Science.** Vol. 48. 2006. 3298-3308.
29. Arenas, M. and J. de Damborenea, *Interference by cerium cations during the multi-step zinc dissolution process in a chloride-containing electrolyte.* **Corrosion Science.** Vol. 48. 2006. 3196-3207.

30. Martínez, L., et al., *Surface study of cerium oxide based coatings obtained by cathodic electrodeposition on zinc*. **Applied Surface Science**. Vol. 257. 2011. 6202.
31. Arurault, L., et al., *Electrochemical preparation of adherent ceria coatings on ferritic stainless steel*. **Thin Solid Films**. Vol. 466. 2004. 75-80.
32. Kobayashi, Y. and Y. Fujiwara, *Effect of SO₄²⁻ on the corrosion behavior of cerium-based conversion coatings on galvanized steel*. **Electrochimica Acta**. Vol. 51. 2006. 4236-4242.
33. Ramezanzadeh, B., H. Vakili, and R. Amini, *Improved performance of cerium conversion coatings on steel with zinc phosphate post-treatment*. *Journal of Industrial and Engineering Chemistry*, 2015. **30**: p. 225-233.
34. Parhizkar, N., B. Ramezanzadeh, and T. Shahrabi, *The epoxy coating interfacial adhesion and corrosion protection properties enhancement through deposition of cerium oxide nanofilm modified by graphene oxide*. *Journal of Industrial and Engineering Chemistry*, 2018. **64**: p. 402-419.
35. Sierra-Fernandez, A., et al., *Synthesis and morpho-structural characterization of nanostructured magnesium hydroxide obtained by a hydrothermal method*. *Ceramics International*, 2014. **40**(8, Part A): p. 12285-12292.
36. Guo, G., et al., *Effect of Synthesizing Temperature on Microstructure and Electrochemical Property of the Hydrothermal Conversion Coating on Mg-2Zn-0.5Mn-Ca-Ce Alloy*. **Metals**. 2016. Vol 6(3).44.
37. Jeong, H. and Y. Yoo, *Synthesis and characterization of thin films on magnesium alloy using a hydrothermal method*. *Surface and Coatings Technology*, 2015. **284**: p. 26-30.
38. Gouadec, G. and P. Colomban, *Raman Spectroscopy of nanomaterials: How spectra relate to disorder, particle size and mechanical properties*. *Progress in Crystal Growth and Characterization of Materials*, 2007. **53**(1): p. 1-56.
39. Shyu, J.Z., W.H. Weber, and H.S. Gandhi, *Surface characterization of alumina-supported ceria*. *The Journal of Physical Chemistry*, 1988. **92**(17): p. 4964-4970.
40. Zhang, Z., et al., *An investigation of the effects of CeO₂ crystal planes on the aerobic oxidative synthesis of imines from alcohols and amines*. **Chinese Journal of Catalysis**. Vol. 36. 2015. 1623-1630.
41. Tiwari, S., et al., *Effect of strain due to Ni substitution in CeO₂ nanoparticles on optical and mechanical properties*. *Scripta Materialia*, 2017. **129**: p. 84-87.

42. Wu, Z., et al., *Probing Defect Sites on CeO₂ Nanocrystals with Well-Defined Surface Planes by Raman Spectroscopy and O₂ Adsorption*. *Langmuir*, 2010. **26**(21): p. 16595-16606.
43. Lee, Y., et al., *Raman analysis of mode softening in nanoparticle CeO_{2-δ} and Au-CeO_{2-δ} during CO oxidation*. *Journal of the American Chemical Society*, 2011. **133**(33): p. 12952-12955.
44. Taniguchi, T., et al., *Tuning Growth Modes of Ceria-Based Nanocubes by a Hydrothermal Method*. *Crystal Growth & Design*, 2011. **11**(9): p. 3754-3760.
45. Tok, A.I.Y., et al., *Hydrothermal Synthesis and Characterization of Rare Earth Doped Ceria Nanoparticles*. *Materials Science and Engineering*. Vol. 466. 2007. 223-229.
46. Klopogge, T., et al., *Infrared and Raman study of interlayer anions CO₂₋₃, NO₃, SO₂₋₄, and ClO₄ in Mg/Alhydrotalcite*. *American Mineralogist*. Vol. 87. 2002. 623-629.
47. Deslouis, C., et al., *Characterization of calcareous deposits in artificial sea water by impedances techniques: 2-deposit of Mg(OH)₂ without CaCO₃*. *Electrochimica Acta*, 2000. **45**(11): p. 1837-1845.
48. Barchiche, C., et al., *Characterization of calcareous deposits in artificial seawater by impedance techniques: 3—Deposit of CaCO₃ in the presence of Mg(II)*. *Electrochimica Acta*. Vol. 48. 2003. 1645-1654.
49. Dawson, P., C.D. Hadfield, and G.R. Wilkinson, *The polarized infra-red and Raman spectra of Mg(OH)₂ and Ca(OH)₂*. *Journal of Physics and Chemistry of Solids*, 1973. **34**(7): p. 1217-1225.
50. Xiuming, Y., et al., *Effect of Heat Treatment on the Corrosion Behavior of AISI 4135 Steel under Natural Seawater Film at Different Temperatures*. *International Journal of Electrochemical Science*. Vol. 9. 2014. 3760-3771.
51. Gabrielli, C., et al., *Study of the Electrochemical Deposition of CaCO₃ by In Situ Raman Spectroscopy I. Influence of the Substrate*. *Journal of The Electrochemical Society*. Vol. 150. 2003. C478-C484.
52. Nguyen Dang, D., et al., *Role of Brucite Dissolution in Calcium Carbonate Precipitation from Artificial and Natural Seawaters*. *Crystal Growth & Design*. Vol. 17. 2017.

Table. 1. Chemical composition of AISI 4135 steel (wt.%)

Elements	C	Si	Mn	Cr	Mo
(wt.%)	0.37	0.4	0.9	1.2	0.3

Figure captions:

Fig. 1. Electrochemical cell used for magnesium hydroxide deposition on ceria coating.

Fig. 2. SEM images of surface **(a)** and cross section **(b)** of CeO₂ coating deposited at -1 mA/cm² during 30 min.

Fig. 3. Raman spectra **(a)** and XRD pattern **(b)** of CeO₂ coating deposited at -1 mA/cm² during 30 min.

Fig. 4. Chronoamperometric curves recorded during the formation of Mg(OH)₂ layer on CeO₂ coating for the both applied potentials.

Fig. 5. SEM surface morphology of Mg(OH)₂/CeO₂ mixed coatings obtained at **(a)** -1V/SCE and **(b)** -1.1V/SCE.

Fig. 6. XRD patterns of Mg(OH)₂ / CeO₂ mixed coatings obtained at both applied potentials.

Fig. 7. SEM images of cross section of Mg(OH)₂/CeO₂ mixed coatings obtained at **(a)** -1V/SCE and **(b)** -1.1V/SCE applied potential.

Fig. 8. EDS cartography of the cross section of Mg(OH)₂/CeO₂ mixed coating obtained at -1,1V/SCE applied potential.

Fig. 9. Raman spectra of the cross section on the internal layer **(a)** and the underneath layer **(b)** of Mg(OH)₂/CeO₂ mixed coating obtained at -1,1V/SCE applied potential.

Fig. 10. **(a)** Open circuit potential evolutions during 6 days of immersion in artificial seawater and **(b)** potentiodynamic polarisation curves after 6 days of immersion of bare steel, CeO₂ coating and Mg(OH)₂/CeO₂ mixed coating.

Fig. 11. **(a)** Rp evolutions of bare steel, CeO₂ coating and Mg(OH)₂/CeO₂ mixed coating during 6 days of immersion in artificial seawater. **(b)** Pictures of the coatings before/After immersion in artificial seawater.

Fig. 12. XRD patterns of **(a)** CeO₂ coating and **(b)** Mg(OH)₂/CeO₂ mixed coating after 6 days of immersion in artificial seawater.

Fig. 13. SEM images of cross-section of CeO_2 coating After 6 days of immersion. **(a)** area that still contains the coating, **(b)** area completely corroded.

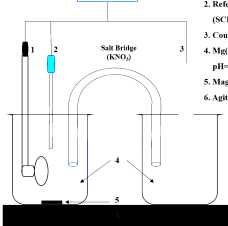
Fig. 14. **(a)** SEM image and **(b)** EDS cartography of cross section of $\text{Mg}(\text{OH})_2/\text{CeO}_2$ mixed coating After 6 days of immersion.

Fig. 15. Raman spectras of cross-section of $\text{Mg}(\text{OH})_2/\text{CeO}_2$ mixed coating After 6 days of immersion in seawater: **(a)** external layer, **(b)** intermediate layer and **(c)** internal layer.

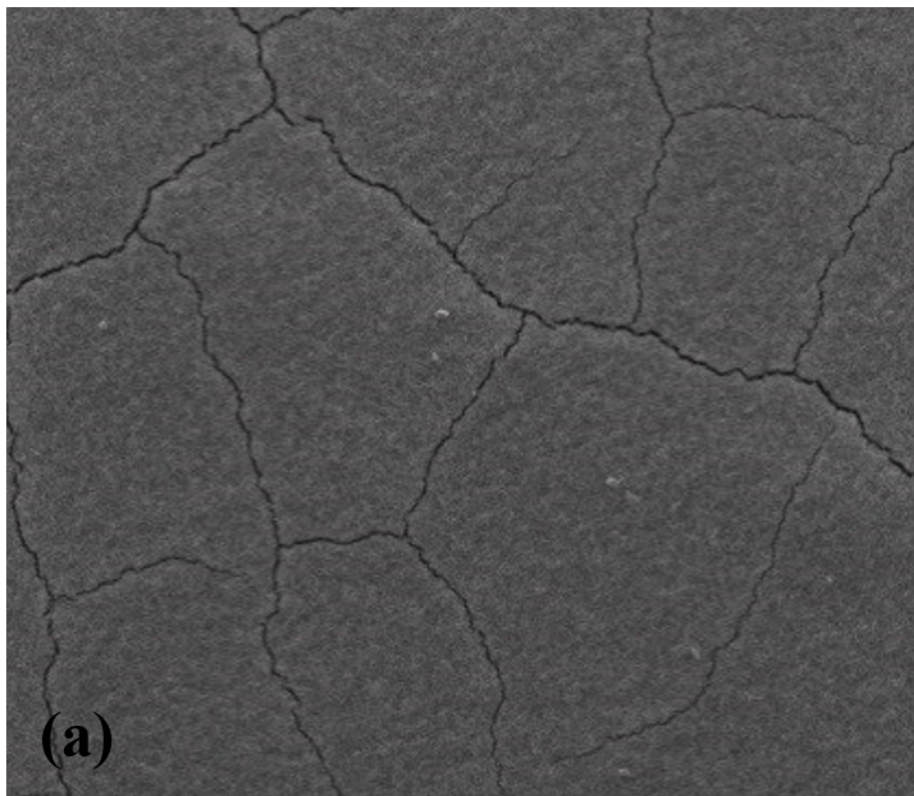
Fig. 16. **(a)** Raman spectras used for the μ -Raman cartography. **(b)** deconvolution of Raman spectra of cerium oxide and magnesium hydroxide.

Fig. 17. **(a)** optical microscope view (objective X50) of cross section of $\text{Mg}(\text{OH})_2/\text{CeO}_2$ mixed coating After 6 days of immersion in seawater. μ -Raman cartography of surrounding by the black quare on picture of the cross section : **(b)** CeO_2 , **(c)** $\text{Mg}(\text{OH})_2$ and **(d)** Aragonite distribution repectively.

**Biologic
VSP**

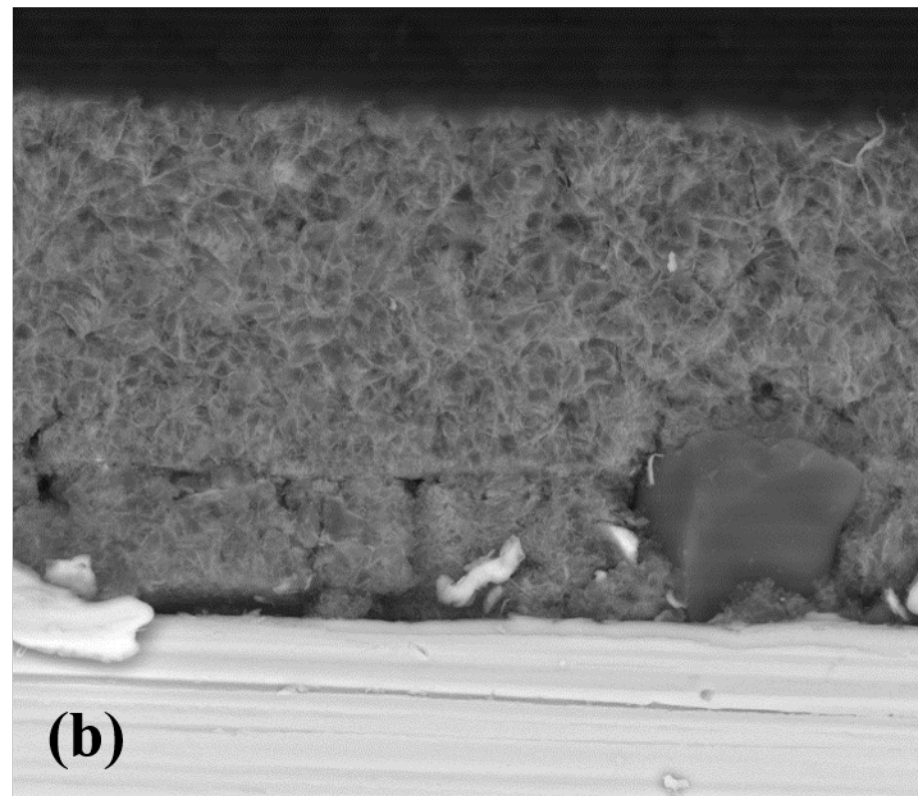


1. Working electrode.
2. Reference electrode (SCE).
3. Counter electrode.
4. $\text{Mg}(\text{NO}_3)_2$, H_2O 0,1M , pH=8,3.
5. Magnetic Stir Bar.
6. Agitator plate.



2/11/2016 HV mag det WD
2:12:55 AM 15.00 kV 400 x ETD 10.2 mm

100 μ m
Univ de Bejaia



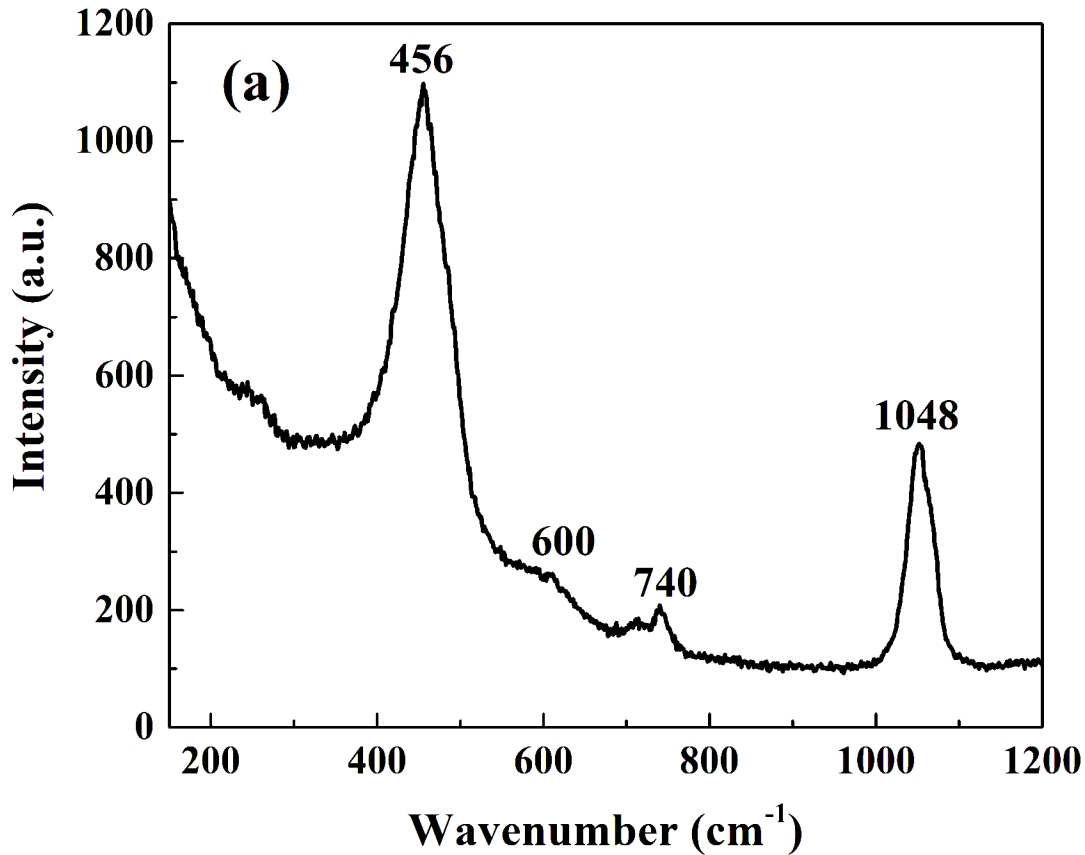
HV Mag Pressure WD Spot
20.0 kV 3000x 0.90 mbar 10.0 mm 3.7

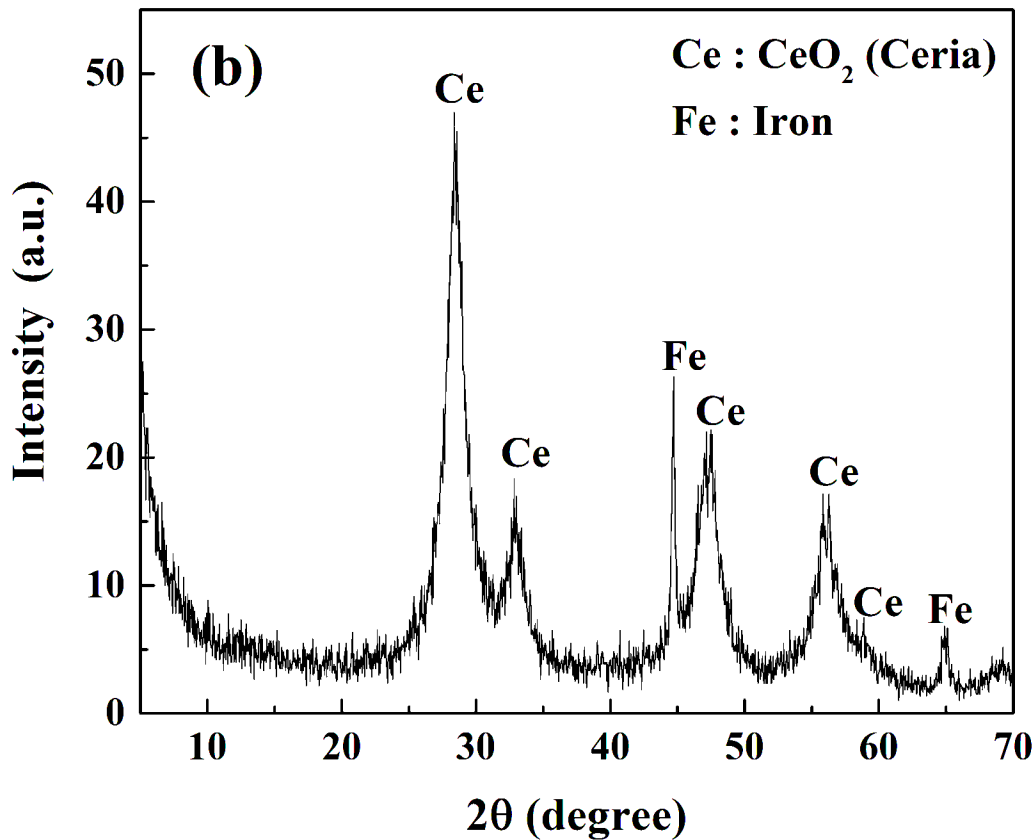
20.0 μ m

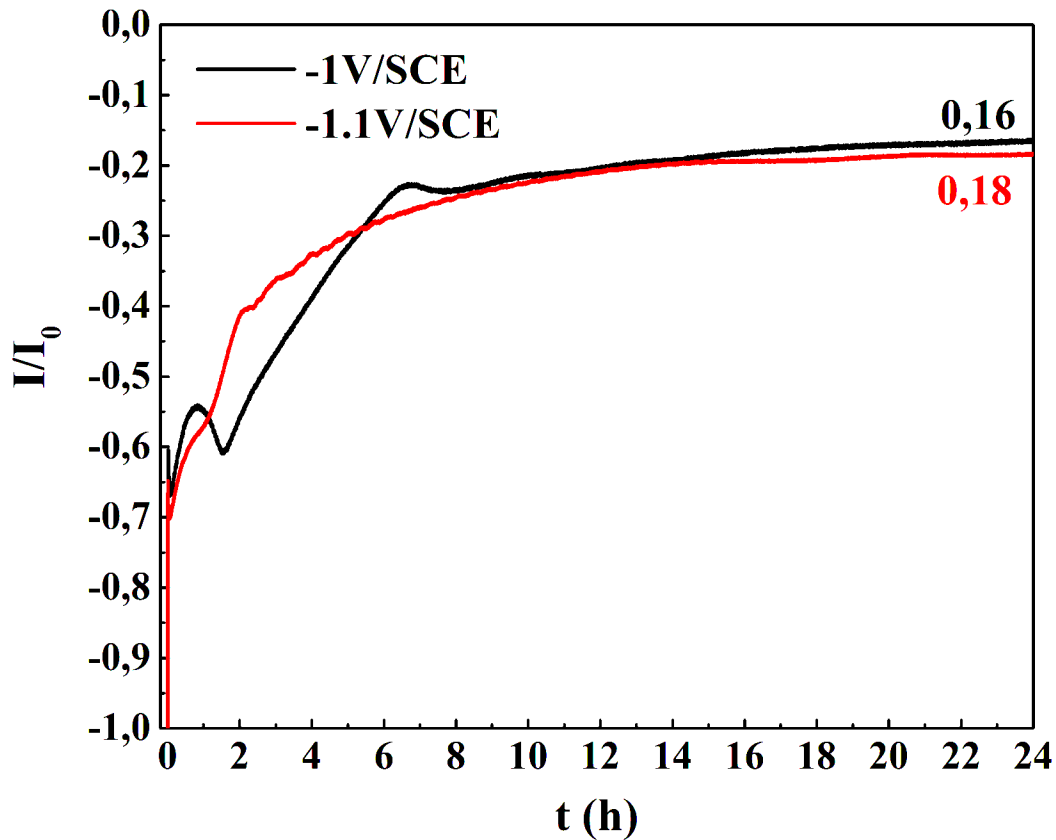
Resin

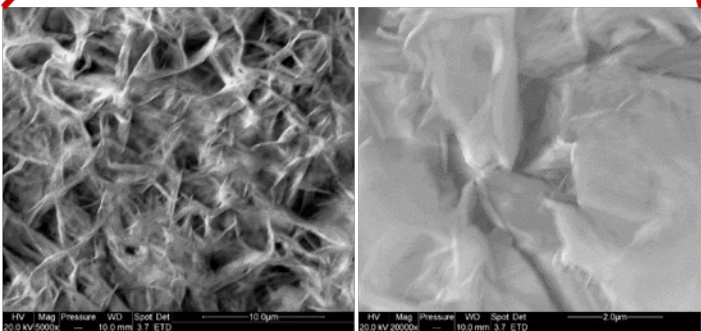
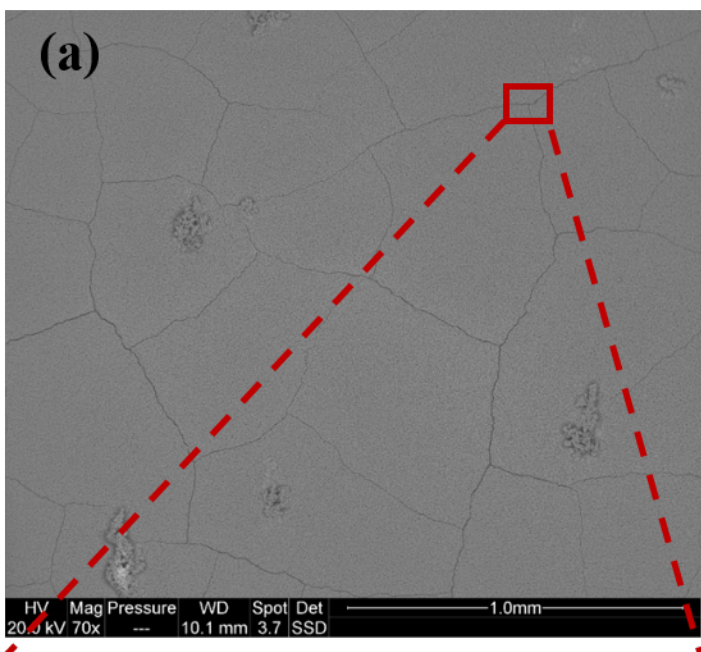
Coating

Substrate



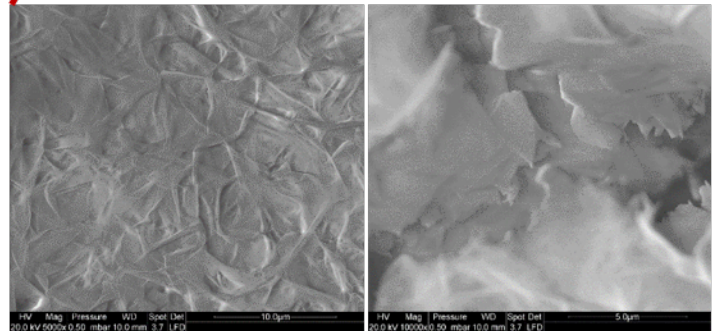
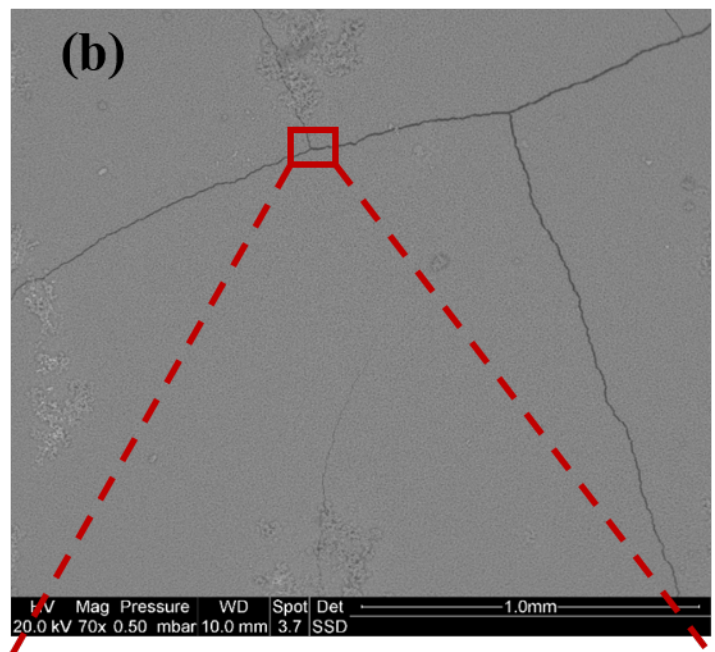






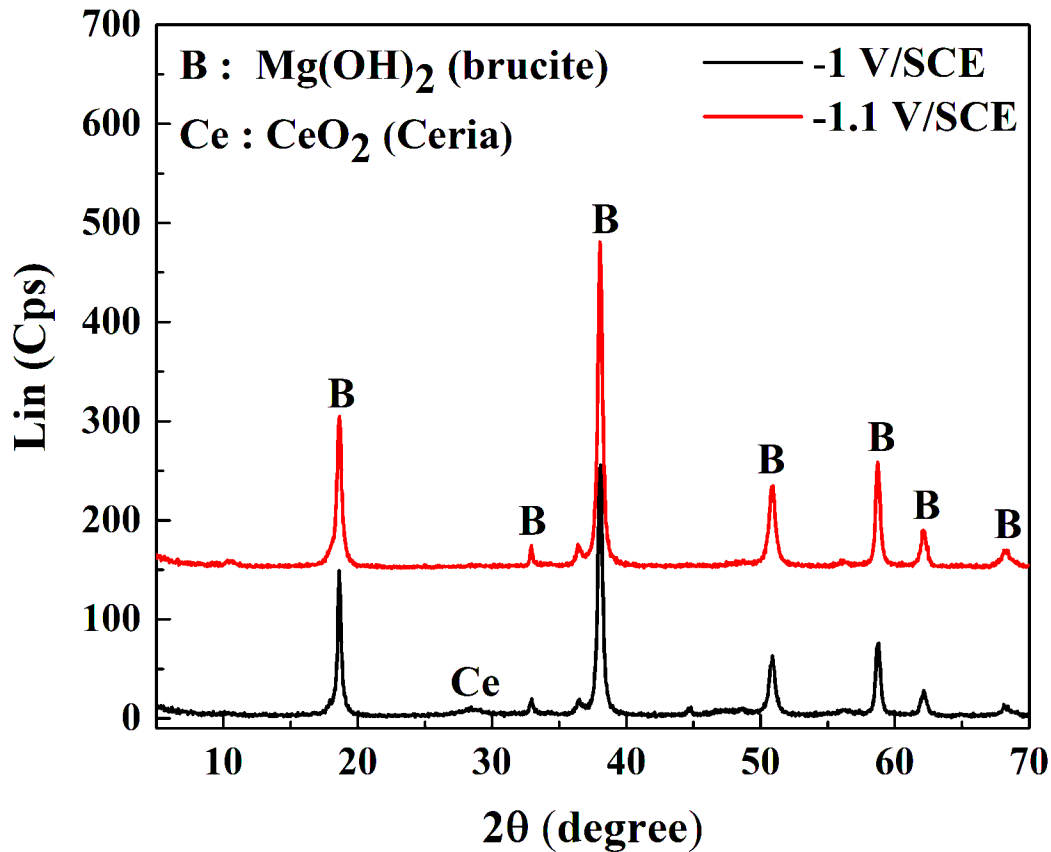
(a.1)

(a.2)

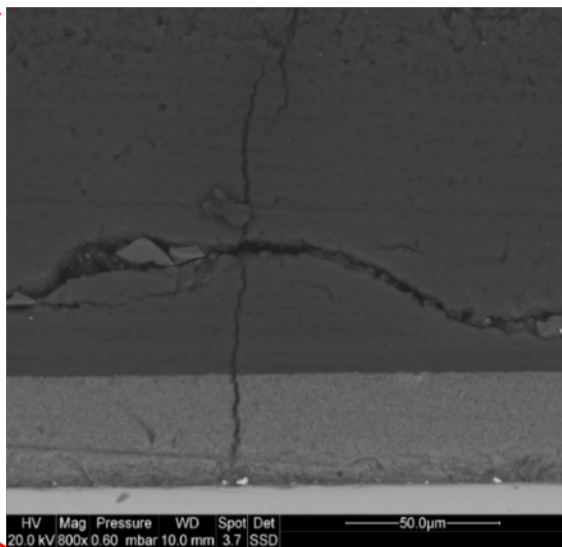
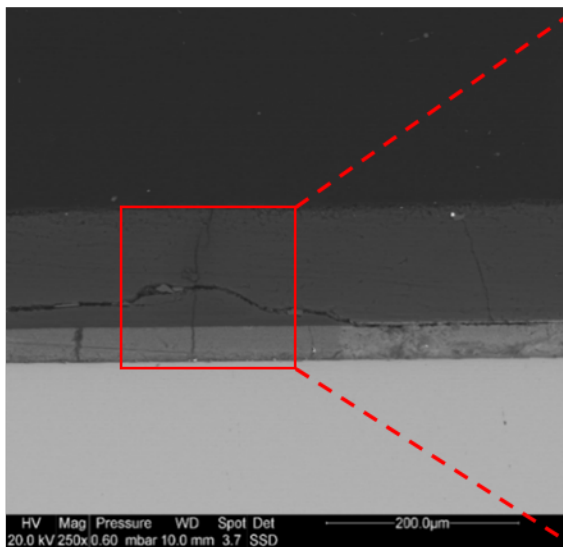


(b.1)

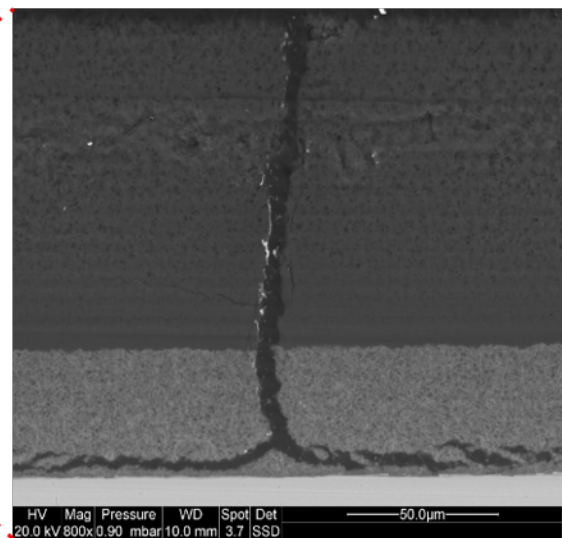
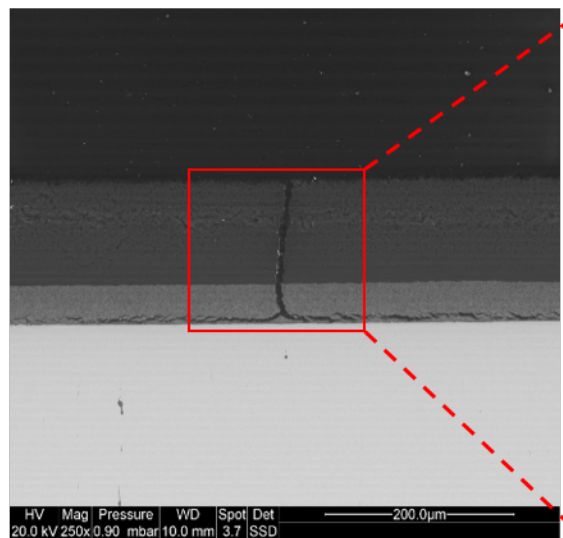
(b.2)

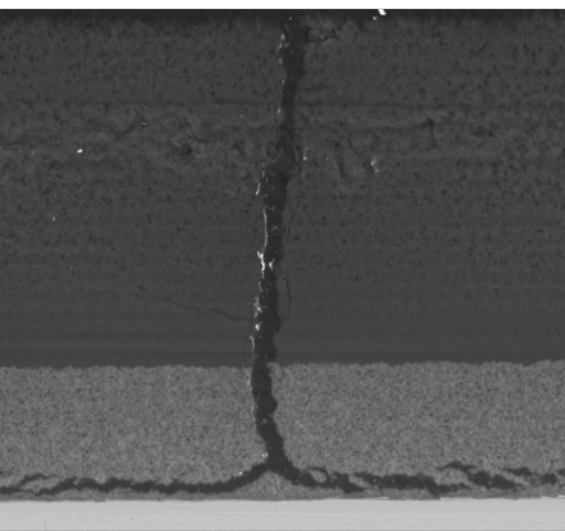


(a)



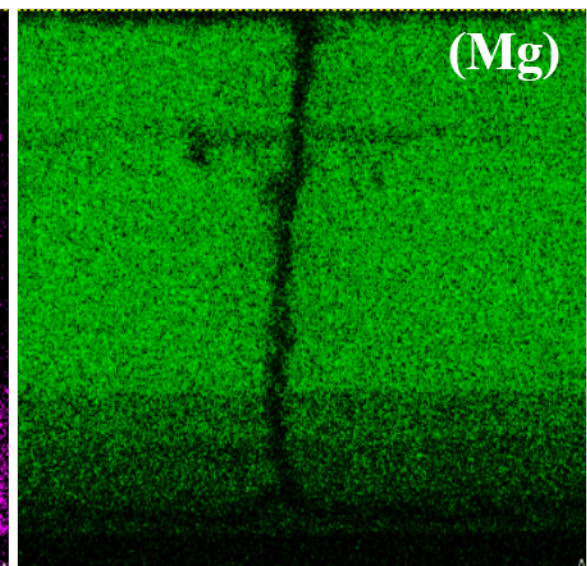
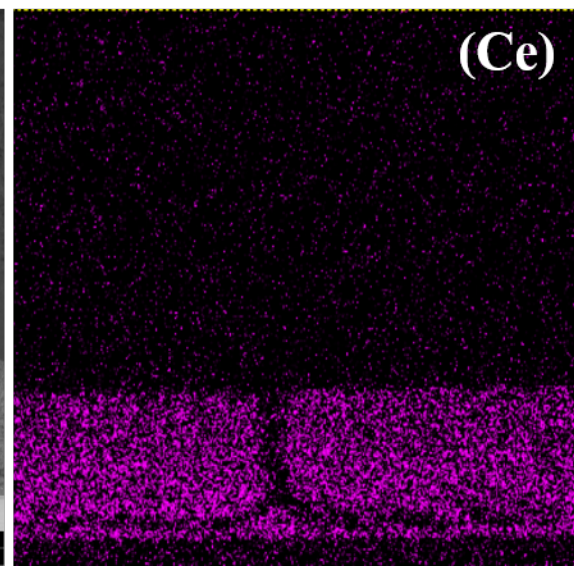
(b)

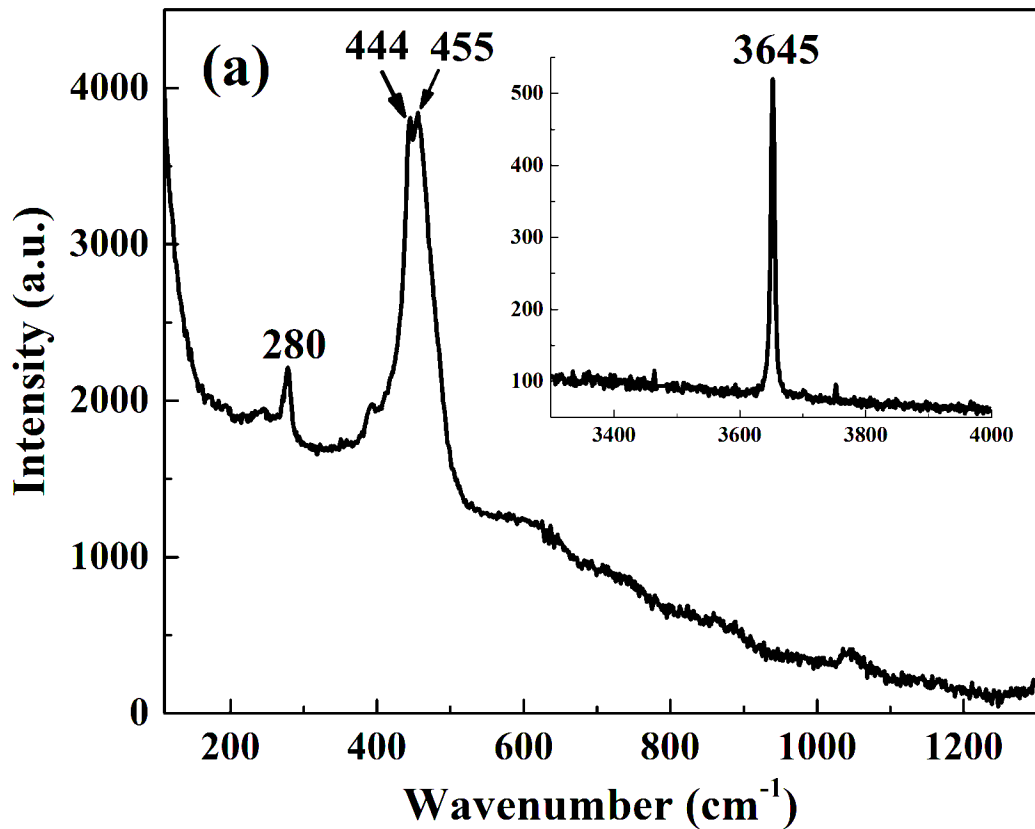


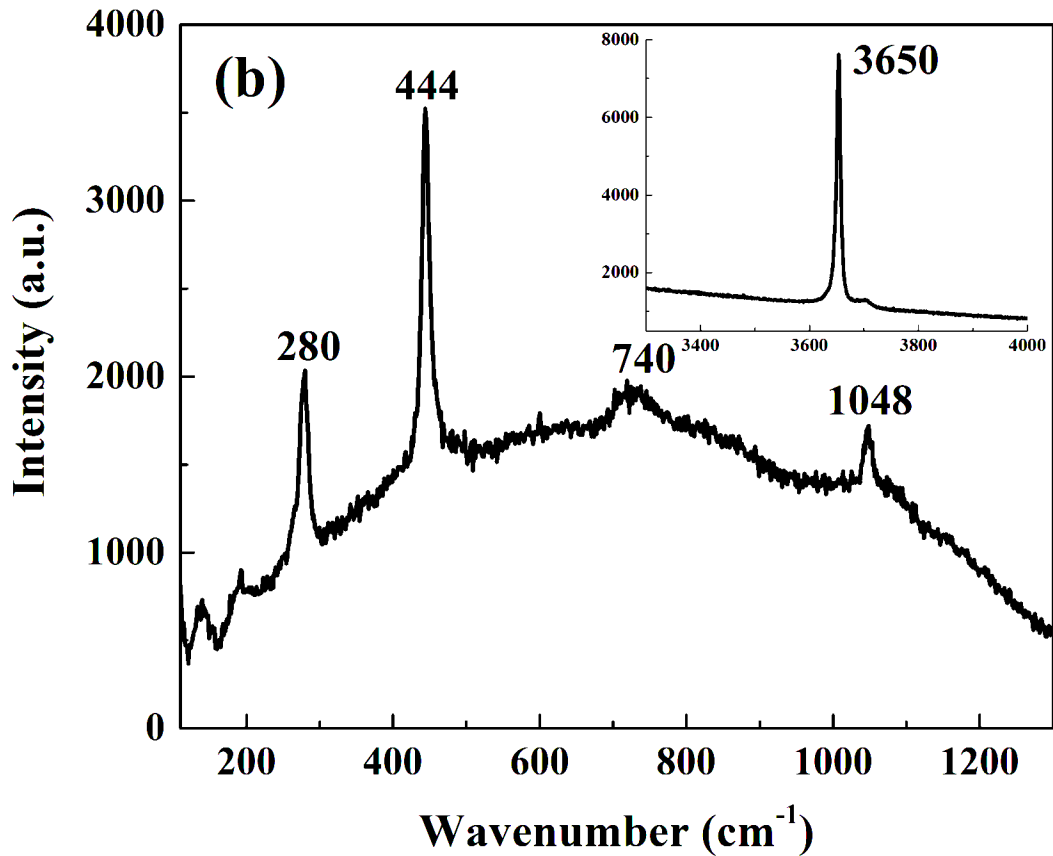


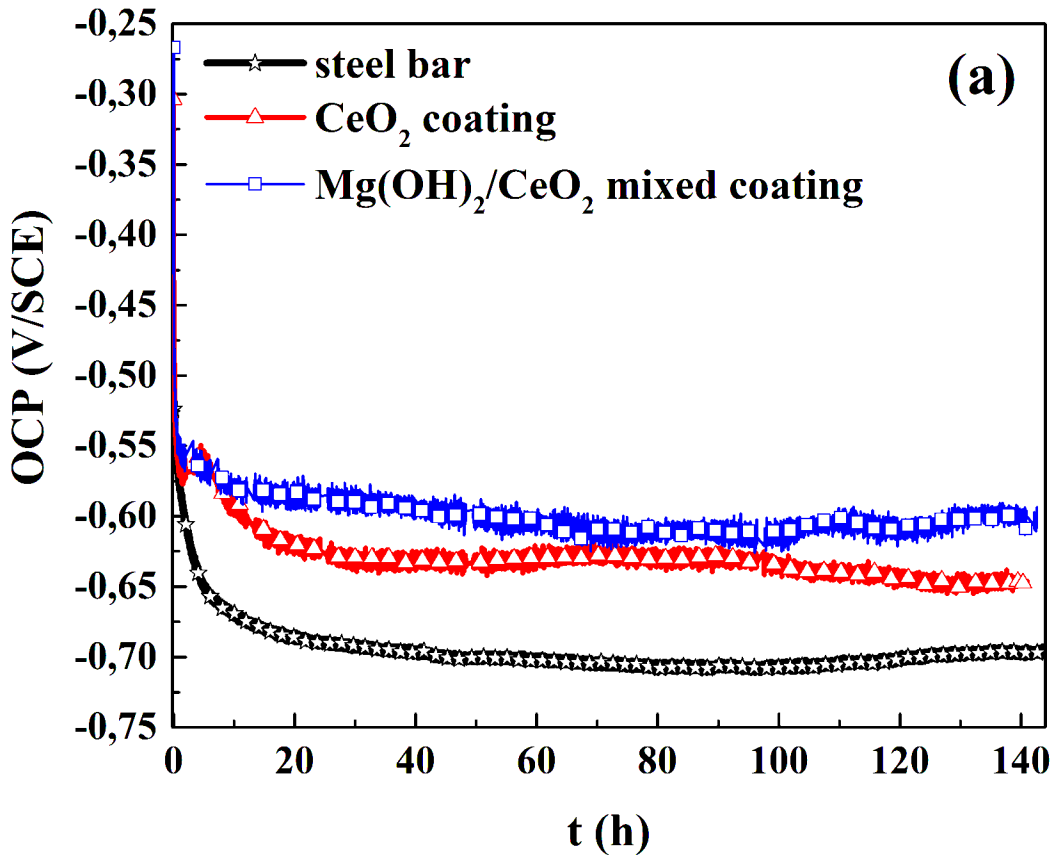
HV	Mag	Pressure	WD	Spot	Det
20.0 kV	800x	0.90 mbar	10.0 mm	3.7	SSD

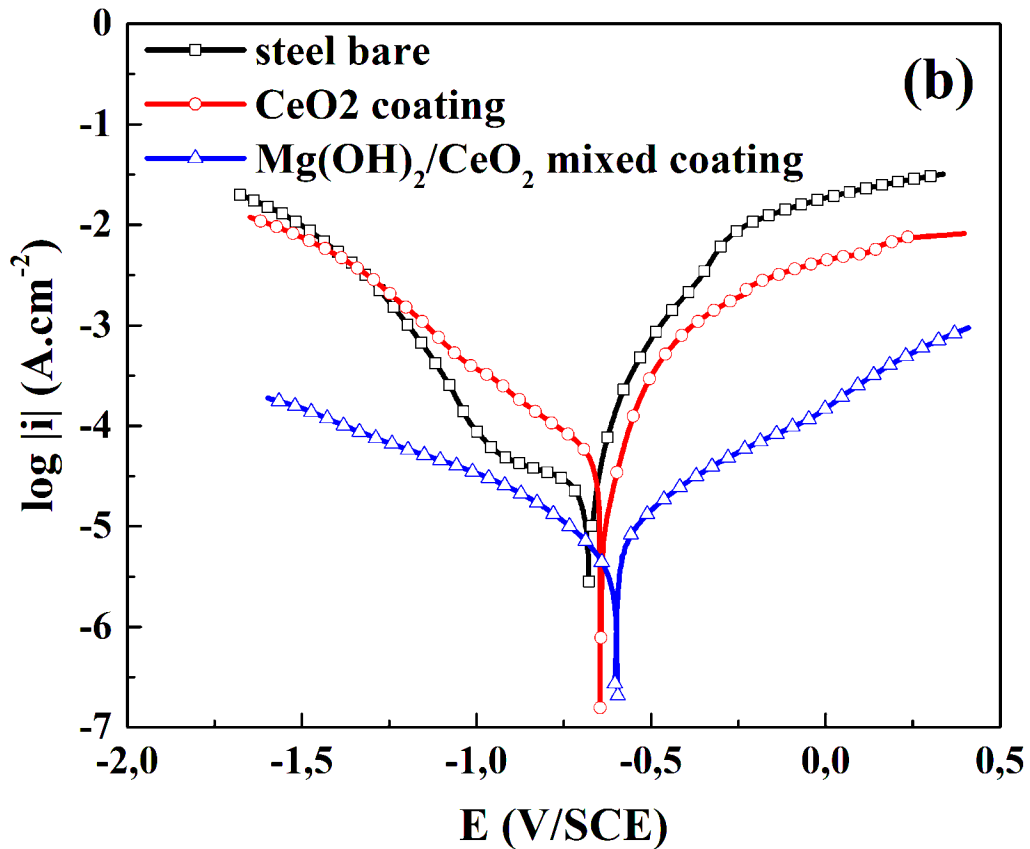
50.0 μm

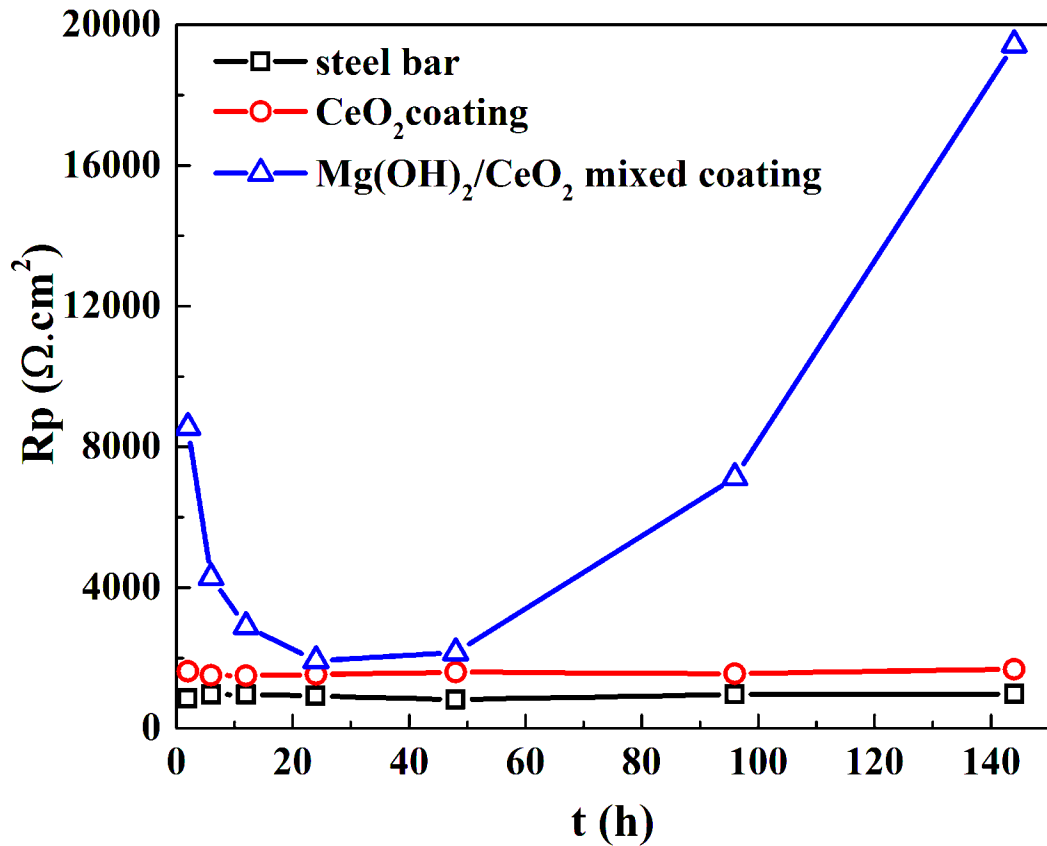










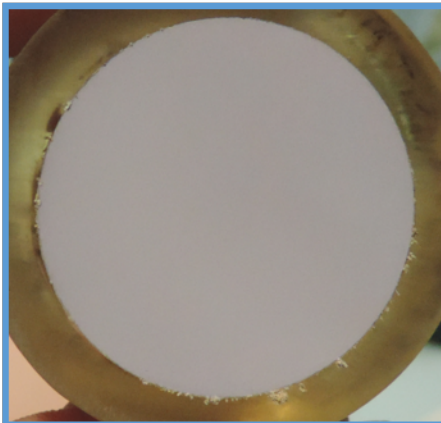


(b)

Before

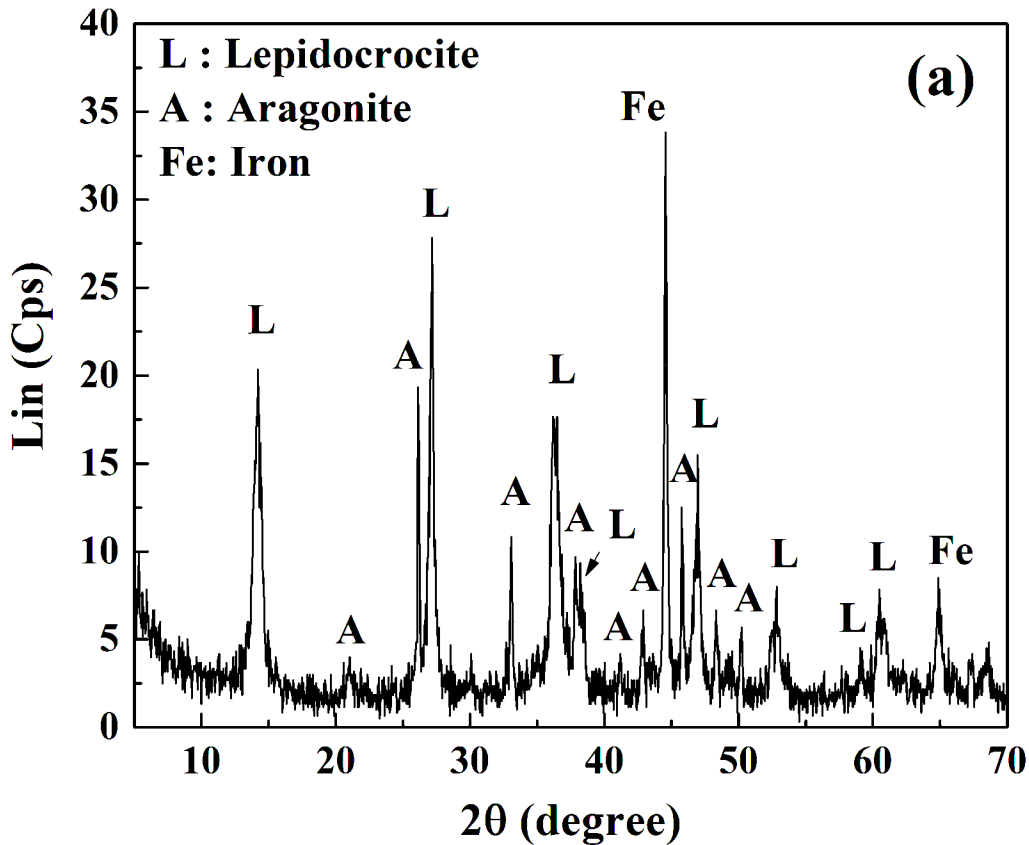
After

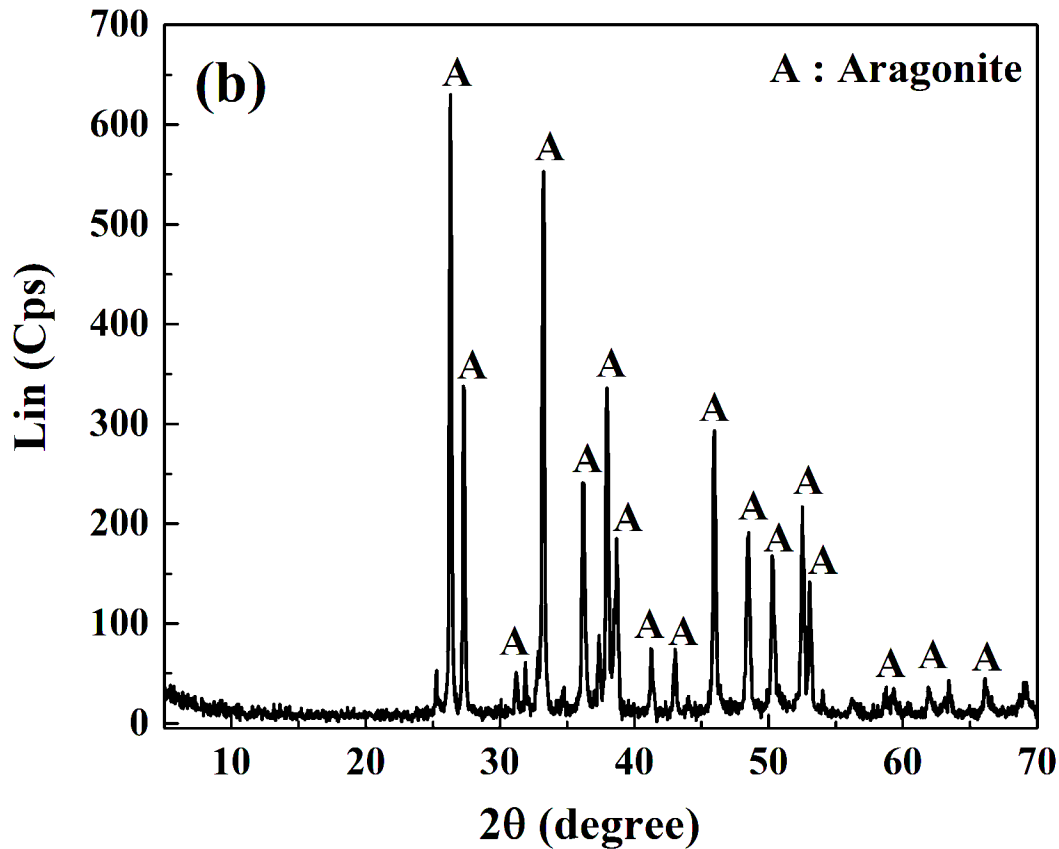
CeO_2
coating

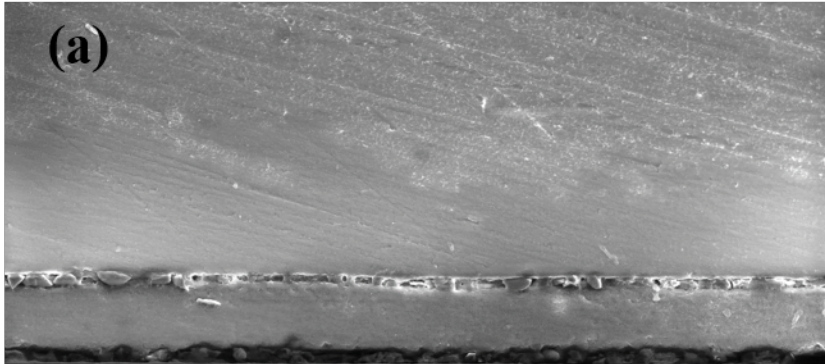


$\text{Mg(OH)}_2/\text{CeO}_2$
mixed coating



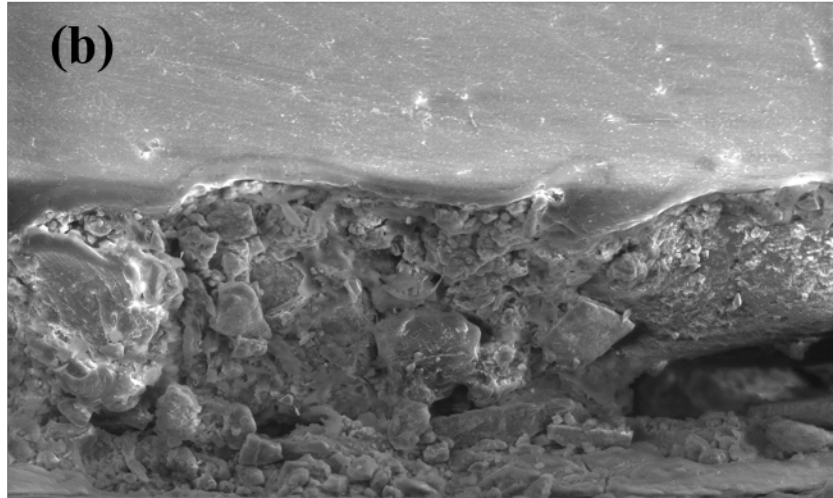




(a)

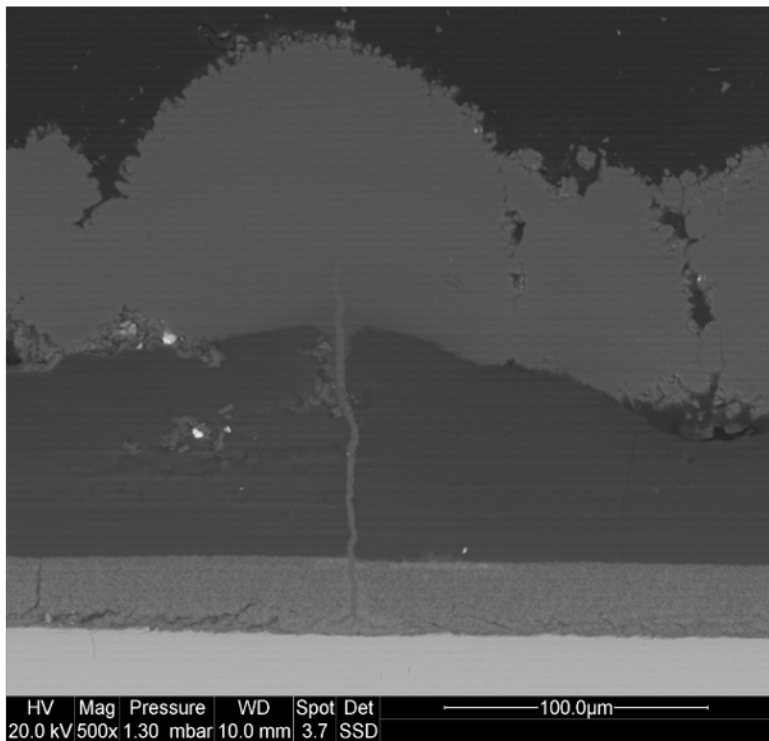
HV	Mag	Pressure	WD	Spot	Det
20.0 kV	300x	0.90 mbar	10.0 mm	3.7	LFD

200.0μm

(b)

HV	Mag	Pressure	WD	Spot	Det
20.0 kV	300x	0.90 mbar	10.0 mm	3.7	LFD

200.0μm

(a)**(b)**